

---

This is an electronic reprint of the original article.  
This reprint may differ from the original in pagination and typographic detail.

Kosulnikov, S.; Diaz-Rubio, A.; Osipov, A. V.; Tretyakov, S. A.

## Experimental Comparison of Anomalous Reflectors Implemented with Local and Non-Local Design Approaches

*Published in:*  
IEEE Transactions on Antennas and Propagation

*DOI:*  
[10.1109/TAP.2024.3451997](https://doi.org/10.1109/TAP.2024.3451997)

Published: 01/01/2024

*Document Version*  
Publisher's PDF, also known as Version of record

*Published under the following license:*  
CC BY

*Please cite the original version:*  
Kosulnikov, S., Diaz-Rubio, A., Osipov, A. V., & Tretyakov, S. A. (2024). Experimental Comparison of Anomalous Reflectors Implemented with Local and Non-Local Design Approaches. *IEEE Transactions on Antennas and Propagation*, 72(10), 7783-7792. <https://doi.org/10.1109/TAP.2024.3451997>

---

This material is protected by copyright and other intellectual property rights, and duplication or sale of all or part of any of the repository collections is not permitted, except that material may be duplicated by you for your research use or educational purposes in electronic or print form. You must obtain permission for any other use. Electronic or print copies may not be offered, whether for sale or otherwise to anyone who is not an authorised user.

# Experimental Comparison of Anomalous Reflectors Implemented With Local and Nonlocal Design Approaches

S. Kosulnikov<sup>1</sup>, A. Díaz-Rubio<sup>2</sup>, *Senior Member, IEEE*, A. V. Osipov, *Senior Member, IEEE*,  
and S. A. Tretyakov<sup>3</sup>, *Fellow, IEEE*

**Abstract**—Developing intelligent radio environments with the ability to engineer and optimize propagation channels has been made possible by metasurfaces that perform anomalous reflection and control the direction of wave reflection at will. Several design methods for creation of anomalous reflectors have been developed, from the simplest locally periodic designs of individual unit cells to advanced global optimizations. In this study, we design, fabricate, and experimentally characterize anomalous reflectors that have the same size and perform the same function but are designed using two different, most commonly used methods. Experimental characterization of the reflector performance over a broad frequency range and for a variety of illumination angles allows comparison of the two methods and helps to select the most suitable design approach for specific application requirements.

**Index Terms**—Angular response, diffraction grating, metasurface, reflection coefficient, scattering.

## I. INTRODUCTION

THERE is a continuous need of enhancing communication systems to make them more effective and versatile as mobile communication technologies evolve. Utilizing intelligent radio environments supported by tunable and programmable metasurfaces is the focus of several recent research initiatives. These technologies can make the propagation channel controllable, programmable, and optimizable, in contrast to typical wireless communication systems where only transmitters and receivers can be optimized. By incorporating adjustable and active elements in the constitutive meta-atoms, metasurfaces enable modifications of their electromagnetic (EM) response and control over wave reflection and transmission.

Manuscript received 8 April 2024; revised 4 August 2024; accepted 26 August 2024. Date of publication 5 September 2024; date of current version 8 October 2024. This work was supported in part by the European Commission through the Horizon 2020 (H2020) Artificial Intelligence Aided D-Band Network for 5G Long Term Evolution (ARIADNE) Project under Grant 871464 and in part by the Research Council of Finland under Grant 345178 and Grant 330957. (Corresponding author: S. Kosulnikov.)

S. Kosulnikov and S. A. Tretyakov are with the Department of Electronics and Nanoengineering, Aalto University, FI-00076 Aalto, Finland (e-mail: sergei.2.kosulnikov@aalto.fi; sergei.tretyakov@aalto.fi).

A. Díaz-Rubio is with the Nanophotonics Technology Center, Universitat Politècnica de València, 46022 València, Spain (e-mail: andiaru@upv.es).

A. V. Osipov is with the Microwaves and Radar Institute, German Aerospace Center (DLR), 82234 Wessling, Germany (e-mail: andrey.osipov@dlr.de).

Color versions of one or more figures in this article are available at <https://doi.org/10.1109/TAP.2024.3451997>.

Digital Object Identifier 10.1109/TAP.2024.3451997

Numerous developments have been made over the past ten years to create metasurfaces that function as anomalous reflectors utilizing various design techniques (e.g., [1], [2], [3], [4], [5], [6], [7], [8]). The improvement of efficiency of reflections into the desired direction has been the primary goal of these investigations. The physics behind these devices and the available design tools are currently well understood. However, it is required to expand this research and take into account aspects that are normally not evaluated in order to integrate these devices into real-world environments. In actual applications, such reflectors may be illuminated from any direction, and their frequency bandwidth is an important performance parameter. For this reason, we will consider not only the response of the metasurfaces at the design conditions but also the angular response and the frequency response to obtain information on how differently designed metasurfaces respond to illuminations at different incidence angles and different frequencies. The goal of this work is to make as complete and full experimental characterization of samples as possible, so that one can compare the reflectors' performances in a wide frequency range and for a wide sector of illumination angles.

The novelty of this work is mainly in experimental characterization of anomalous reflectors that have the same size and perform the same function but are designed using two different, most commonly used methods. We target at identifying differences in the properties of reflectors designed based on different physical principles at various illuminations in a wide angular and frequency range. To the best of our knowledge, this kind of experimental characterization and comparison has been made here for the first time. Known works focus on one design (local or nonlocal) and performance for the design incident angle and for the desired operational frequency or its close vicinity. Here, we present the first comparative experimental study of two designs based on comprehensive measurements over all angles and in a very broad frequency range. In particular, we report on experimental investigations of two samples of anomalous reflectors that differ only by the used design method. To enable comparison of effects due to the different design approaches, we design and manufacture both samples at the same platform: the same substrate material and thickness, the same number of unit cells in each supercell, the same basic shape of meta-atoms, and the same

manufacturing technique. Let us also note that most of the known experimental studies of anomalous reflectors (this is an active field of study in view of the prospects of developing reconfigurable intelligent surfaces, RIS) focus on far-field measurements of the fields scattered from finite-size panels, while, here, we measure the macroscopic reflection coefficients that physically characterize the reflection properties of panels and can be used in analytical estimations of finite-size panel performance at any observation angle.

The structure of this article is as follows. We begin by outlining the implementation strategies for each sample that is being studied. Next, we describe the measurement setup. Finally, we compare anomalous reflection capabilities of the reflectors under study in terms of both angular and frequency response with experimental and numerical results. The conclusion section finalizes this article.

## II. IMPLEMENTATION OF ANOMALOUS REFLECTORS USING PERIODICAL METASURFACES

Devices called anomalous reflectors can change the direction in which waves travel upon reflection from flat panels. These devices can be realized as periodic arrays (diffraction gratings) whose period is determined by the desired angles of incidence and reflection, or as reflectarrays whose geometrical period is fixed usually to  $\lambda/2$ . Impenetrable metasurfaces—periodic structures that block the fields behind the metasurface and enable reflected waves to flow in various directions that coincide with Floquet harmonics—offer the most flexible way to design anomalous reflectors. The Floquet–Bloch theory states that the  $n$ th mode propagates with the transverse wavevector  $k_{xn} = k_0 \sin \theta_i + (2\pi n/D_x)$ , where  $\theta_i$  defines the direction of propagation of the incident plane wave and  $D_x$  is the period of the structure, as illustrated in Fig. 1(a).

The dispersion relation in free space for each harmonic defines the normal component of the wavevector as  $k_{zn}^2 = k_0^2 - k_{xn}^2$  and, thus, the direction of propagation of reflected waves. Depending on the period, the excitation frequency, the incident angle, and the harmonic order, Floquet modes can propagate in free space if  $|k_{xn}| < k_0$ , i.e., if  $k_{zn}$  is real. For those modes, the direction of propagation can be found from

$$\theta_{rn} = \arcsin \left( \sin \theta_i + \frac{2\pi}{k_0 D_x} n \right) \quad (1)$$

where the values of  $\theta_{rn}$  are the reflection angles of the propagating harmonics of indices  $n = 0, \pm 1, \pm 2, \dots$ . Using this relation, one can determine the period required for scattering energy into the desired direction.

The complex amplitude of each excited Floquet harmonic,  $A_n$ , is determined by the specific microstructure of the period, and its ratio to the amplitude of the incident wave is referred to as the macroscopic reflection coefficient [9]. The magnitude of the macroscopic reflection coefficient of the mode propagating in the desired direction determines the efficiency of the anomalous reflector. In general, the amount of power channeled into each propagating Floquet harmonic for TE polarization can be calculated as follows:

$$P_m = |A_n|^2 \frac{\cos \theta_{rn}}{\cos \theta_i}. \quad (2)$$

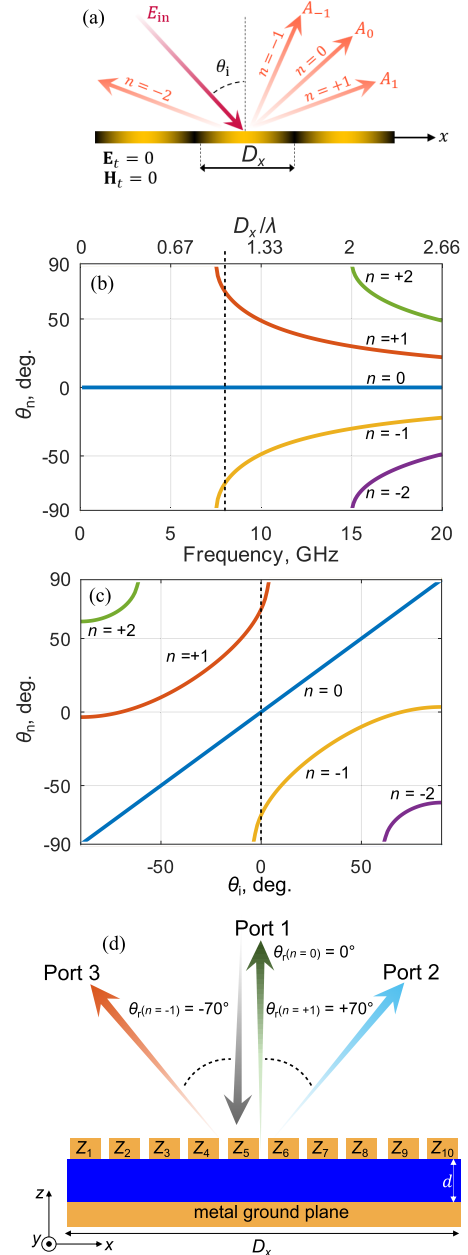


Fig. 1. (a) Generalized conceptual illustration of wave scattering from an infinite impenetrable periodic metasurface with period  $D_x$ . (b) Scattered diffracted harmonics directions as the functions of the frequency (bottom  $x$ -axis) or  $D_x/\lambda$  (top  $x$ -axis). (c) Scattered diffracted harmonics directions as the functions of the incidence angle  $\theta_i$ . Vertical dashed lines show the design parameters selected in this study. (d) Conceptual illustration of scattering from metasurfaces under normal illumination analyzed.

The design strategies for creation of anomalous reflectors using metasurfaces can be divided into two main groups: *local designs* that assume that the response of each constitutive element only depends on the fields at the exact position where the element is placed, and *nonlocal designs* that account for interaction between different meta-atoms and optimize them to channel the energy toward the desired harmonic(s).

### A. Local Design Methodology

In local designs, such as reflectarrays [10], [11], [12] or local metasurfaces [13], [14], the local reflection phase is

varied along the reflector surface, so that the partial waves reflected from each array element interfere constructively in the desired reflection direction. The desired local reflection coefficient dictated by the phased-array principle, also referred to as the generalized reflection law, can be written as  $\Gamma(x) = 1 \cdot e^{jk_0(\sin\theta_i - \sin\theta_{rd})x}$ , where  $\theta_{rd}$  represents the desired reflection angle. In this method, the unit cells are designed using the locally periodical approximation, usually by numerically simulating periodic arrays of identical cells. It is well known that these implementations suffer from parasitic scattering when the relation between the incidence and reflection angles significantly deviates from the usual reflection law for uniform reflectors (e.g., [2], [3]).

A test prototype for the anomalous reflector based on the local design approach was designed for operation at 8 GHz, for  $\theta_i = 0^\circ$ , and  $\theta_{r1} = 70^\circ$ . Fixing the operational frequency and the desired reflection, we get the required periodicity  $D_x = 40$  mm of the structure from (1). The results of higher order mode reflections under normal illumination are shown in Fig. 1(b), where the vertical dashed line indicates the selected operational frequency, and the first order reflection  $n = \pm 1$  from the infinite periodical structure is toward  $\theta_{r\pm 1} = \pm 70^\circ$ . The  $n = \pm 1$  harmonics become propagating at frequencies above  $\sim 7.52$  GHz for the selected design parameters. This observation also assures that higher order harmonics with  $n = \pm 2$  are only excited at frequencies above  $\sim 15.04$  GHz.

The supercell consists of ten rectangular copper patches above a copper ground plane. The width of all the patches is  $w = 3.5$  mm. The thickness  $d$  of the dielectric substrate is 1.575 mm, and the final dimensions of each supercell in the  $xy$  plane are  $D_x = 40$  mm and  $D_y = 18.75$  mm.

Additional analytical investigation of our selected periodicity with (1) may be done by varying the illumination angle. The results presented in Fig. 1(c) show the propagation directions of higher order harmonics for the structure illuminated at different angles  $\theta_i$  and the operational frequency 8 GHz. Harmonics of the order  $n = \pm 2$  are excited for illumination angles  $|\theta_i| > 61.5^\circ$ , whereas at other illumination angles, the reflection angles become complex valued; i.e., the exited reflected harmonics with  $n = \pm 2$  are nonpropagating. For the illumination angle range,  $\theta_i \approx (\pm 3.5^\circ, \pm 61.5^\circ)$  harmonics with order  $n = \pm 1$  are nonpropagating; i.e., only two propagating harmonics are exited.

The resulting conceptual design of anomalous reflectors operation under normal illumination is shown in Fig. 1(d). When the structure is illuminated normally, three propagating harmonics are excited, toward  $0^\circ$ ,  $+70^\circ$ , and  $-70^\circ$ . The structure consists of a dielectric supporting substrate, and two metallized layers: back metal ground plane, and top layer of metal patches or meta-atoms, designed to provide the required grid impedance of the top layer.

The first step in the design based on the local phase gradient is to determine the dimensions of each meta-atom that produce the desired reflection phase. To do that, we used the conventionally employed locally periodical approximation. We conducted a full-wave EM analysis with ANSYS HFSS and simulated the reflection coefficient for single periodically

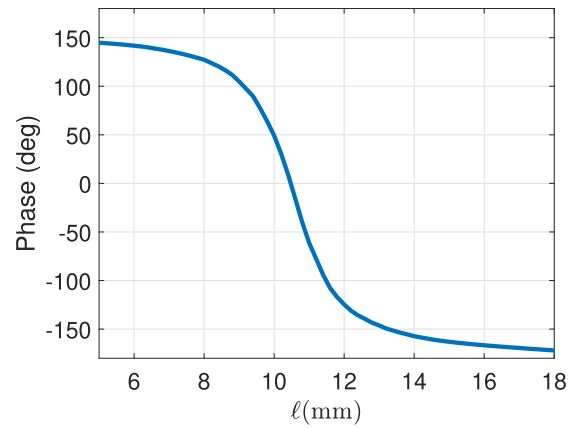


Fig. 2. Parametric study of the local reflection coefficient phase as a function of the patch length.

repeated array elements (single patches on the grounded substrate) at normal incidence and found the lengths of the patches that produce the desired phase shift at the position of each array element within the period  $d_x = D_x/10$ . The simulation domain was  $D_x/10 \times D_y \times 2\lambda$  (along the  $x$ -,  $y$ -, and  $z$ -directions). The dielectric substrate the simulations had  $\epsilon_r = 2.2$ ,  $\tan\delta = 0.0009$ , and thickness  $t = 1.575$  mm. The rectangular patches and the ground plane were modeled as copper ( $\sigma = 58 \times 10^6$  S/m) with a thickness of  $70 \mu\text{m}$ . In Fig. 2, one can see the results of a parametric study of the local reflection coefficient phase as a function of the length of the patches. To provide a linear phase gradient  $\Phi(x) = k_0(\sin\theta_i - \sin\theta_{r1})x$  along each period of the metasurface, the final dimensions of the patches are  $l_1 = 10.78$  mm,  $l_2 = 11.17$  mm,  $l_3 = 11.57$  mm,  $l_4 = 12.62$  mm,  $l_5 = 18$  mm,  $l_6 = 5$  mm,  $l_7 = 8.8$  mm,  $l_8 = 9.6$  mm,  $l_9 = 10.12$  mm, and  $l_{10} = 10.52$  mm. The experimental sample comprises 11 supercells along the  $x$ -axis and 14 supercells along the  $y$ -axis and has the size of  $11.7\lambda = 440$  mm and  $7\lambda = 262.5$  mm, respectively. A photograph of the sample designed with the local approach is shown in Fig. 3(a), and a schematic representation of the top-view of one supercell is shown in Fig. 3(b).

Because the incidence and reflection angles are different, the plane-wave impedances of the incident and reflected waves, defined as the ratios of the tangential (to the reflector) components of the electric and magnetic fields, are different. This impedance mismatch between the incident plane wave and the required reflected waves limits the efficiency of anomalous reflectors based on the linear phase gradient design, as was shown, e.g., in [4]. The following expression can be used to calculate the expected efficiency of a design based on the difference between the incident angle and reflected angle in the lossless scenario [3]:

$$\eta = 4 \frac{\cos\theta_i \cos\theta_{r1}}{(\cos\theta_i + \cos\theta_{r1})^2}. \quad (3)$$

The anomalous reflector prototype designed for  $\theta_i = 0^\circ$  and  $\theta_{r1} = 70^\circ$  by using the local design approach has a theoretical efficiency of 75.96% according to (3). For actual samples,

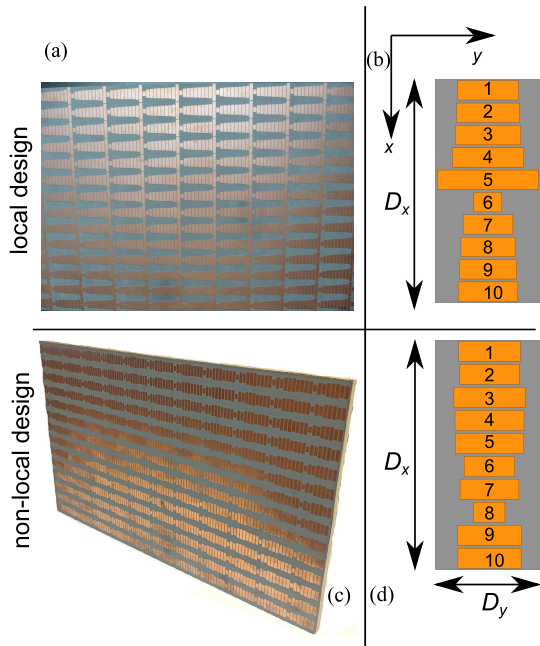


Fig. 3. Implemented anomalous reflectors under study. (a) Local design sample photograph, (b) its supercell, (c) nonlocal design sample photograph, and (d) its supercell.

this efficiency will be reduced due to the effects of losses in materials and inaccuracies in manufacturing.

We implemented an anomalous reflector with the described local design methodology as an infinite planar reflector in a full-wave EM simulation. In this case, the ten-element supercell is set with periodic boundaries across the  $xy$  plane. Floquet modes are associated as Ports 1–3 shown in Fig. 1(d). As a result, we get relations between the amplitudes of the incident and reflected Floquet modes of various orders. The resulting simulated scattering matrix of the infinite structure, considering losses in all used materials as described above, reads

$$|S_{\text{sim}}^{\text{loc}}| = \begin{bmatrix} 0.261 & \mathbf{0.835} & 0.444 \\ 0.835 & 0.029 & 0.541 \\ 0.444 & 0.541 & 0.681 \end{bmatrix}. \quad (4)$$

In terms of the power reflection efficiency, the structure offers 69.71% anomalous reflection efficiency with 3.81% of absorption. The rest of the energy is scattered into other Floquet harmonics. In particular, 19.67% of incident power is sent into the  $n = -1$  mode (that corresponds to  $-70^\circ$ ), and 6.81% is sent into the  $n = 0$  mode (normal reflection).

### B. Nonlocal Design Methodology

To overcome the intrinsic limitations of anomalous reflectors based on the locally periodic approximation and linear phase gradient, one has to employ strong nonlocalities [4], [6], [15], use evanescent fields behind or above the metasurface to optimize the power flow along the reflector surface [1], [16], or adapt the shape of the metasurface to the power modulation [7]. These solutions have demonstrated that parasitic reflections can be eliminated, and only losses in materials

reduce the efficiency of the anomalous reflectors, overcoming the limitations dictated by (3).

In this article, to make a comparison between local and nonlocal designs, we compare the characteristics of samples fabricated with the same technology and the same number of elements per supercell. More specifically, we design an anomalous reflector using the nonlocal approach [4], keeping the same design conditions with an operation frequency of 8 GHz,  $\theta_i = 0^\circ$ , and  $\theta_{r1} = 70^\circ$ . For the implementation, all the physical dimensions of the sample are the same ( $w = 3.5$  mm, the thickness  $d$  of the dielectric substrate is 1.575 mm, and the total dimensions of each supercell in the  $xy$  plane are  $D_x = 40$  mm and  $D_y = 18.75$  mm) except for the length of the patches. The dimensions of each component in the unit cells of the linear phase gradient design are used as an initial guess for numerical optimization of the structure. The entire simulation domain of the supercell was  $D_x \times D_y \times 2\lambda$ . The quasi-Newton (gradient) algorithm was applied, and  $|S_{11}| = 1$  was set as the objective. The final dimensions of the patches are  $\ell_1 = 10.7$  mm,  $\ell_2 = 10.3$  mm,  $\ell_3 = 12.3$  mm,  $\ell_4 = 12$  mm,  $\ell_5 = 11.8$  mm,  $\ell_6 = 8.7$  mm,  $\ell_7 = 10.2$  mm,  $\ell_8 = 5.4$  mm,  $\ell_9 = 11$  mm, and  $\ell_{10} = 10.9$  mm. This is the same design as presented in [4]. In this design, the lengths of the metallic patches were numerically optimized using commercial software to maximize the reflection in the desired direction. A photograph of the samples is shown in Fig. 3(c), and a schematic representation of the top view of one supercell is shown in Fig. 3(d). The resulting amplitudes of the simulated scattering matrix components of the infinite structure, considering losses in all used materials as described above, read

$$|S_{\text{sim}}^{\text{nonloc}}| = \begin{bmatrix} 0.030 & \mathbf{0.980} & 0.037 \\ 0.980 & 0.026 & 0.030 \\ 0.037 & 0.030 & 0.969 \end{bmatrix}. \quad (5)$$

In terms of the power reflection efficiency, the nonlocally implemented structure results in 96.06% anomalous reflection efficiency, and 3.72% is dissipated in the reflector. The rest of the energy is scattered into other Floquet harmonics. In particular, 0.13% is sent into the  $n = -1$  mode (that corresponds to  $-70^\circ$ ), and 0.09% is sent into the  $n = 0$  mode (that corresponds reflection in the normal direction). Notice that similar design strategies can be used with dielectric resonators. At microwave frequencies, the resonators can be made, for example, with polymer-based high-permittivity ceramics placed on a ground plane [17].

### III. MEASUREMENT SETUP

For the experimental characterization of the samples, we used a setup that allows us to extract the macroscopic reflection coefficients or, in other words, the scattered power sent into the propagation direction of each Floquet harmonic. The objective is to study the angular response and the frequency response in the Cx- and X-bands, namely, from 6.5 to 9.9 GHz, to cover a sufficiently large frequency range around the design frequency of both structures at 8 GHz. The measurements were carried out at the Microwaves and Radar Institute, German Aerospace Center (DLR), Oberpfaffenhofen,

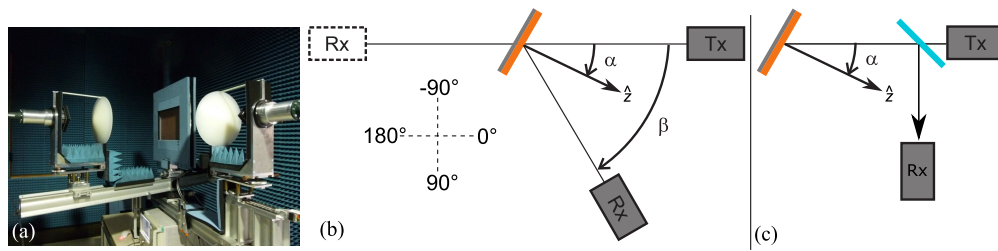


Fig. 4. Measurement setup. (a) Photograph of the setup in an anechoic laboratory environment, (b) schematic of a bistatic measurement, and (c) schematic of a monostatic measurement. Here,  $\alpha$  is the rotation angle of the reflector, and  $\beta$  is the bistatic angle.

Germany. A photograph of the experimental setup is shown in Fig. 4(a). Horn antennas with dielectric lenses served as the transmitting and receiving units. The transmitting unit (Tx) was in a fixed location and illuminated the samples with a beam with a roughly planar wavefront. The beam diameter was approximately 11 cm. The lens at the receiving unit (Rx) permitted selection of the reflected waves propagating from the illuminated spot on the sample toward the receiver along the antenna axis. The focused beams formed by lenses at the horns excluded the unwanted contributions from the edges of the samples. The reflectors were mounted on a holder that had a frame of  $41 \times 25$  cm covered by a microwave absorber. The setup allows rotation of the sample at an angle  $\alpha$  with respect to the transmission unit.

Measurements were conducted for both bistatic and monostatic scattering analysis. For bistatic measurements, the receiving unit and the sample could be independently rotated at the angles  $\alpha$  and  $\beta$  around a common vertical rotation axis; see Fig. 4(b). The bistatic angle between Tx and Rx can be adjusted between  $180^\circ$  (direct talk) and  $30^\circ$ . However, due to mechanical restrictions with the lenses, smaller bistatic angles could not be set. Therefore, in the monostatic scenario (bistatic angle  $0^\circ$ ), a combined Tx/Rx block was used, with Tx and Rx at a right angle to one another and separated by a semi-transparent power divider (a glass plate); see Fig. 4(c). The thickness of the glass plate is optimized to divide the energy of the incident wave in such a way that both the transmitted and reflected waves are attenuated by approximately 3 dB in the case of normal incidence. In the case of  $45^\circ$  incidence, the attenuation values are approximately 5 dB (transmission and TE polarization, and reflection and TM polarization) and 1.5 dB (transmission and TM polarization, and reflection and TE polarization). Different antenna units were used for the Cx- and X-bands frequency ranges.

A schematic representation of the measurements conducted with the bistatic arrangement is shown in Fig. 4(b). The system was calibrated with  $\beta = 30^\circ$  and a metal plate with its normal pointing in the direction  $\alpha = 15^\circ$ , i.e., in the direction of specular reflection. The following parameters have been varied during the measurements: 1) bistatic angle  $\beta$  between  $30^\circ$  and  $180^\circ$  with a step of  $5^\circ$ ; 2) reflector rotation angle  $\alpha$  between  $-60^\circ$  and  $90^\circ$  with a step of  $1^\circ$ ; and 3) frequency between 6.5 and 8.2 GHz (Cx-band) and between 8.202 and 9.9 GHz (X-band) with a step of 2 MHz.

In addition, measurements were conducted for two positions of each reflector: position  $0^\circ$  [with the  $x$ -axis oriented as in Fig. 3(b) and (d)] and position  $180^\circ$  obtained by rotation of

the sample by  $180^\circ$  around the unit normal  $\mathbf{z}$  to its surface, Fig. 4(b) and (c), to account for the whole range of incidence directions, because the arrangement of the inclusions on the metasurfaces is not symmetric with respect to the surface normal.

In the monostatic measurements, a single Tx/Rx unit ( $\beta = 0^\circ$ ) was used. The reflector rotation angle  $\alpha$  in this case was varied between  $-60^\circ$  and  $40^\circ$  with a step of  $1^\circ$ . A schematic of the measurements conducted with the monostatic arrangement is shown in Fig. 4(c). The monostatic measurement system was also calibrated with a metal plate at broadside illumination ( $\alpha = 0^\circ$ ), and the measurement is provided for the same two frequency bands as in the bistatic measurement.

The gathered raw datasets are 2-D arrays of the magnitude, phase, real, and imaginary components of the reflected signal in the monostatic measurement case (sweeps over frequency and the angle  $\alpha$ ) and 3-D arrays in the bistatic scenario (sweeps over frequency and the angles  $\alpha$  and  $\beta$ ).

#### IV. DATA PROCESSING, RESULTS, AND DISCUSSION

To obtain the response of the metasurface according to the configuration shown in Fig. 1, we use the following relations:  $\theta_i = \alpha$  and  $\theta_{\text{obs}} = \beta - \alpha$  for position  $0^\circ$ . For position  $180^\circ$ , we have  $\theta_i = -\alpha$  and  $\theta_{\text{obs}} = -(\beta - \alpha)$ . Here,  $\theta_{\text{obs}}$  denotes the observation angle that defines the position of the receiving antenna with respect to the metasurface normal.

As a result, we get 2-D datasets at each frequency, which were interpolated to construct sets with a similar  $1^\circ$  step along both  $\theta_i$  and  $\theta_{\text{obs}}$  axes. An example of raw data collected at the design frequency 8 GHz is presented in Fig. 5 for the reference metal mirror and two anomalous reflectors under study. The shown data are limited for the range  $[-90^\circ, 90^\circ]$  for both  $\theta_i$  and  $\theta_{\text{obs}}$ , as only the top (patterned) side of the reflectors is of interest.

The reference metal mirror has maximum reflection toward specular direction—the maximum is always observed at  $\theta_{\text{obs}} = \theta_i$ . Both anomalous reflectors confirm the designed functionality, since the maximum of reflection is observed at  $\theta_{\text{obs}} = 70^\circ$  when  $\theta_i = 0$ . In the discussed 2-D data, we can follow exactly the same response of modes allocation as predicted by the theoretical results shown in Fig. 1(c); i.e., maximized  $n = 0$  specular mode reflected from conventional metal mirror is shown in Fig. 5(a) as a similar straight line contour, and contours of both anomalous  $n = \pm 1$  modes are clearly seen reflected from anomalous reflectors in Fig. 5(b) and (c). White gaps in the 2-D figures indicate the areas where no scattering

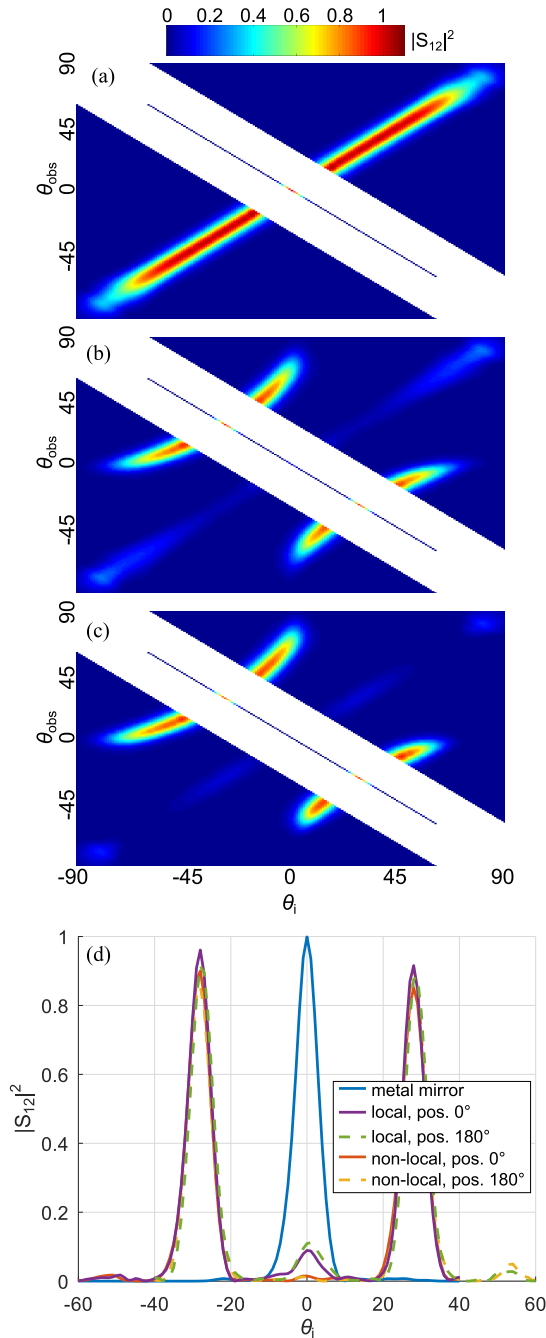


Fig. 5. Processed measurement results at 8 GHz with the experimental setup presented in Fig. 4. (a)–(c)  $|S_{12}|^2$  of the metal reference plate, local design, and nonlocal design, accordingly, built in the range of observation and incidence angles  $[-90^\circ, 90^\circ]$  and (d) same types of data but for the monostatic measurement cut.

measurement were possible because of the measurement setup limitations (the angle between Tx and Rx cannot be smaller than  $30^\circ$ ). The contributions from the higher order modes with  $n = \pm 2$  could not, therefore, be observed. However, for the modes with  $n = \pm 1$ , scattering toward anomalous directions is clearly defined. Also, it is evident that for the local design methodology, the parasitic specular scattering is more pronounced, comparing with the nonlocal implementation.

The thin line in the middle of the white gap in Fig. 5(a)–(c) shows retroreflection data provided by the

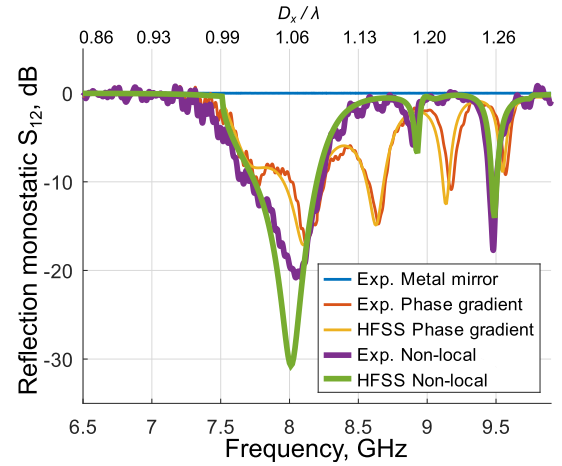


Fig. 6. Experimental results according to the monostatic measurement setup presented in Fig. 4(c) for  $\alpha = 0^\circ$  and the corresponding infinite reflectors simulation results as a function of frequency.

monostatic measurement. For more convenient observation, these data are shown separately in Fig. 5(d). These data were collected two times for two sample positions ( $0^\circ$  and  $180^\circ$ ) in the measurement. Thus, both orientation-related lines are shown in Fig. 5(d). Overlapping of these lines regardless of possible spot shifts due to sample orientation changes confirms sufficiently high quality of manufacturing of the reflectors and accuracy of the measurements.

#### A. Retroreflection Frequency Response Under Normal Illumination

We start by analyzing the response of the metasurface for the design conditions, i.e., illuminated at normal incidence. First, we consider the frequency dependence of the reflection coefficient into the normal direction (specular reflection). We set  $\theta_{\text{obs}} = \theta_i = 0^\circ$ , which corresponds to normal illumination, i.e.,  $\alpha = 0$  in the monostatic measurement; see Fig. 4(c). The results of the measurement are presented in Fig. 6. The experimental results are accompanied also with the related EM simulations and show the amplitude of scattering toward retroreflection, i.e., for the observation point located at the normal from the illuminated surface. We also verified that the EM simulation result is symmetrical over the  $xz$  plane; thus, only one line is presented here.

We can observe a clear minimum in the retroreflection from normally illuminated reflectors (that is, in specular reflection) for both samples near the design frequency point 8 GHz. This minimum indicates that the energy is not reflected back toward the transmitter but rather is redirected to another direction and/or could also be dissipated. The sample based on the local design shows weaker minima comparing with the nonlocal reflector. For the experimental data, a particular shift of the resonance minima toward higher frequencies is observed for both experimentally implemented reflectors. Precise positions of the minima are shown in Table I. For the local implementation, the shift is stronger than for the nonlocal reflector. Measurements at higher frequencies show a noticeable difference between the designs in terms of resonances positions. We will discuss this in more detail at the end of this section.

TABLE I  
PRECISE POSITIONS OF MINIMA FOR THE MONOSTATIC MEASUREMENT FROM THE RESULTS PRESENTED IN FIG. 6

Local design				Non-local design			
position 0°		position 180°		position 0°		position 180°	
$f$	$D/\lambda$	$f$	$D/\lambda$	$f$	$D/\lambda$	$f$	$D/\lambda$
8.116	1.0796	8.114	1.0793	8.046	1.0703	8.084	1.0754
8.646	1.1501	8.648	1.1504	8.896	1.1834	8.896	1.1834
9.176	1.2206	9.172	1.2201	9.48	1.2611	9.472	1.2600
9.57	1.2730	9.57	1.2730	n/a	n/a	n/a	n/a

### B. Frequency Dependence of Anomalous Reflection Efficiency Toward Fixed Observation Points Under Normal Illumination

The macroscopic reflection coefficient is calculated as the measured reflection coefficient from the metasurface normalized by that for specular reflection from the reference metallic mirror plane illuminated under a reference angle  $\theta_{\text{ref}}$

$$r_0 = \frac{S_{12}^{\text{MS}}(\theta_i, \theta_{\text{rn}})}{S_{12}^{\text{mirror}}(\theta_{\text{ref}}, \theta_{\text{ref}})}. \quad (6)$$

For extreme illumination angles, the illumination spot projected over the finite sample becomes larger than the sample area, and some part of the illumination power misses the surface and is not reflected toward the receiver. Therefore, the reference angle  $\theta_{\text{ref}}$  is selected as the largest angle out of  $\theta_i$  and  $\theta_{\text{obs}}$

$$\theta_{\text{ref}} = \begin{cases} \theta_i, & \text{if } \theta_i \geq \theta_{\text{obs}} \\ \theta_{\text{obs}}, & \text{if } \theta_i < \theta_{\text{obs}}. \end{cases} \quad (7)$$

This normalization ensures the highest reflection level that can be obtained from a perfect reflector illuminated under the reference angle. The reflection efficiency  $\eta$  is found as the second power of the absolute value of  $r_0$ :  $\eta = r_0^2$ .

We start our analysis of bistatic scattering fixing the observations points. As it was mentioned before, under normal illumination, this scenario allows propagation of three Floquet harmonics  $n = -1, 0$ , and  $1$  that correspond to the reflection angles equal to  $-70^\circ$ ,  $0^\circ$ , and  $70^\circ$  at the operation frequency of 8 GHz. For the case of infinite metasurface simulation with the fixed supercell periodicity, the directions of the reflected Floquet harmonics are frequency-dependent. If the receiving antenna is located at fixed observation directions  $\theta_{\text{obs}} = -70^\circ$ ,  $0^\circ$ , and  $+70^\circ$  and the illumination is normal  $\theta_i = 0^\circ$ , the measured results may be directly compared with the infinite metasurface simulation only at the design frequency. The results for scattering from the metasurfaces toward these fixed observation directions are presented in Fig. 7(a) and (c). The figures show the efficiency as a function of the frequency. The design frequency 8 GHz, corresponding to anomalous reflection for the desired maximized harmonic  $n = +1$ , is shown with the point marker. The results are in a very good agreement with the estimations from EM simulations, which were discussed in Sections II-A and II-B.

Next, we consider the ranges where the efficiency of the anomalous reflection is greater than 50%. For the local design, the measured range is 7.69–8.47 GHz. For the nonlocal design, half-power or higher anomalous reflection efficiency is observed in the experimental data in the range 7.66–8.28 GHz. Another important note here is that for both samples, the

maximum of anomalous reflection efficiency is detected when the observation point is shifted a bit toward higher frequencies: for the local implementation, the maximum is at 8.17 GHz, and for the nonlocal implementation, it is at 8.03 GHz. Further analysis of this aspect will be performed in Section IV-D.

### C. Angular Response

In this section, we study the response of the metasurface when it is illuminated at different angles. We show how the energy is distributed between the different propagating Floquet harmonics by extracting the macroscopic reflection coefficient both numerically and experimentally.

The results of the normalized scattered power magnitude toward  $n = -1, 0, +1$  harmonics for the local and nonlocal designs are presented in Fig. 7(b) and (d). Experimental points are shown as crosses, and the EM simulated results for the corresponding infinite structures are shown by solid lines. In EM simulations for the incidence angles  $\theta_i > 61^\circ$ , the harmonic with  $n = -2$  makes a noticeable contribution, which, however, could not be extracted from the measured results due to the mentioned above setup limitations. Obviously, the experimentally extracted points for  $\theta_i = 0^\circ$  correspond to the frequency-dependent curves presented in Fig. 7(a) and (c) at the design frequency. Precise efficiency values at these design points are shown with curve tips. We see a good qualitative coincidence between the numerical simulations and the experimental data for the measured harmonics.

The results indicate a considerably higher impact of parasitic scattering toward  $n = -1$  and  $0$  for the local design sample. Another noticeable feature of the nonlocal implementation is the dependency of the results outside of the design configuration illumination. For illumination angles interval  $0^\circ < |\theta_i| < 30^\circ$ , we see minima for  $n = \pm 1$  harmonics and maxima for  $n = 0^\circ$  harmonic, whereas for the local implementation, the shapes of the curves are reversal. Sharp drop of efficiency when illumination is slightly shifted from normal is in line with Fig. 1, because the related scattered harmonic's reflection angle becomes complex.

### D. Frequency Response

In order to determine the scattered harmonics amplitudes in the case that the periodicity of the structure is fixed, we have to select the observation angle related to the investigated frequency in accordance with (1). The result for the scattered harmonics amplitudes, taking into account this angular correction factor, is presented in Fig. 8. An additional  $x$ -axis on top of the figure indicates the corresponding  $\theta_{\text{rn}}$  for  $n = \pm 1$ . In this

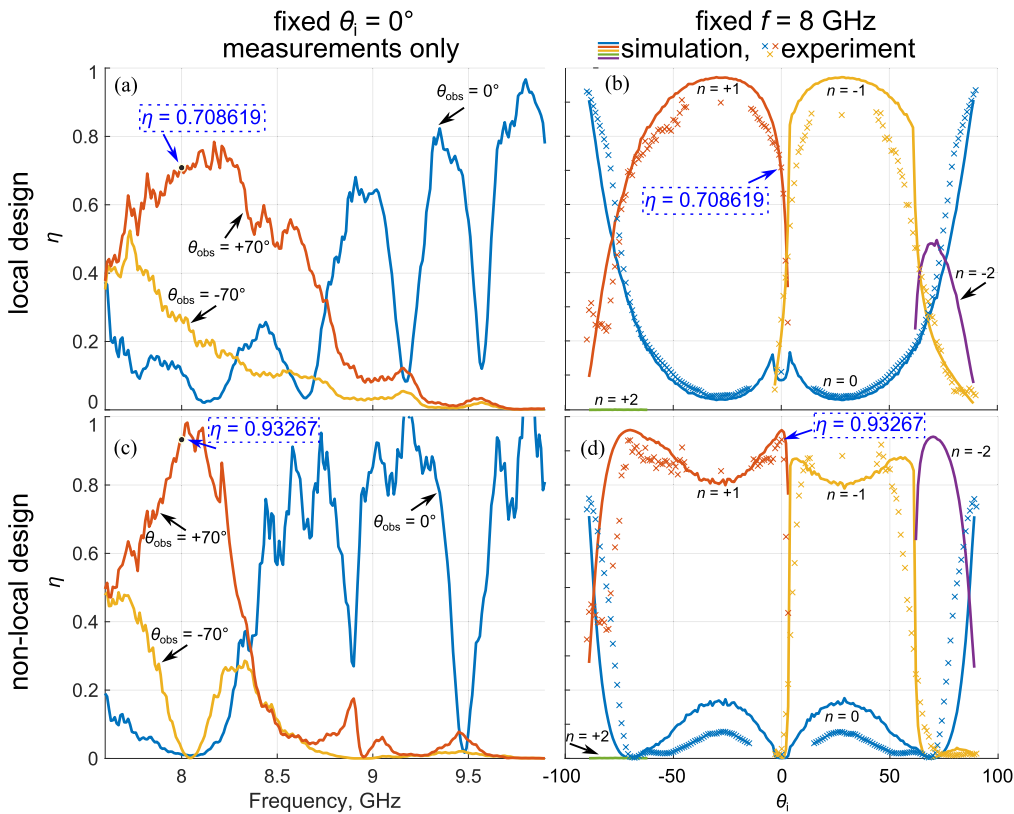


Fig. 7. Normalized scattered power magnitude: (a) and (b) local design and (c) and (d) nonlocal design. (a) and (c) Correspond to the case, when the observation angles of the scattered harmonics are fixed (for normal incidence), and the operational frequency varies (experimental results only). (b) and (d) Correspond to the case when the operational frequency is fixed to 8 GHz, and the incidence angle is varied (both simulation and experimental data). Marker tips show precise measured efficiency at the design frequency and illumination angle. The colors of the curves correspond to the scheme used in Fig. 1(b) and (c).

case, the efficiency results can be directly compared with the EM simulations of infinite structures; thus, the results in Fig. 8 are accompanied with the curves showing calculated data.

In the case of the local design, from the result presented in Fig. 8(a), one can see a broad operational range of anomalous reflection toward the target angle of  $70^\circ$ , with the efficiency value close to the theoretical maximum for this design (about 75%) at the design frequency marked with a point marker. The measured efficiencies at the design frequency are shown above the dashed lines. In the case of the nonlocal implementation presented in Fig. 8(b), one can see almost perfect efficiency at the design frequency, but the frequency bandwidth of this anomalous reflector is somewhat narrower. The bandwidths where the efficiency of anomalous reflection to the  $n = +1$  mode is larger than 50% for the local design read the following.

- 1) *Simulation*: 7.7–8.74 GHz with the peak  $\eta = 76.25\%$  at 8.12 GHz.
- 2) *Measurement*: 7.8–8.78 GHz with the peak  $\eta = 83.39\%$  at 8.17 GHz.

For the nonlocal design, the corresponding results are as follows.

- 1) *Simulation*: 7.66–8.25 GHz with the peak  $\eta = 96.16\%$  at 7.99 GHz.
- 2) *Measurement*: 7.77–8.28 GHz with the peak  $\eta = 97.81\%$  at 8.02 GHz.

The first difference between both design that we can see is in the deviation of the maximum efficiency frequency from the theoretical prediction. In the nonlocal design, the maximum efficiency is expected at the design frequency, and the measurements indeed show only a small shift toward higher frequencies (0.03 GHz) that can be a consequence of inaccuracies in fabrication or a deviation in the material properties between the actual values and the theoretical assumption. In the local design, the simulated maximum efficiency does not appear at the design frequency, but at 8.12 GHz. To understand this frequency shift, one should remember that local designs are not exact solutions of the boundary-value problem for inhomogeneous arrays, and excitation of additional evanescent fields that match the boundary conditions is required. Additional evanescent fields store some reactive energy, which is equivalent to an additional surface reactance that causes a frequency shift, not accounted for in the local design. Thus, in this design, these evanescent fields couple energy with the first Floquet harmonic more efficiently at higher frequencies. This effect cannot be predicted or controlled at the design stage.

It is important to notice that the difference of the maximal efficiency frequency between simulations and experiments is of the same order for both local and nonlocal designs (0.05 and 0.03 GHz). Because the materials and fabrication process were the same for both samples, this confirms that this small deviation is due to inaccuracies in fabrication or a deviation

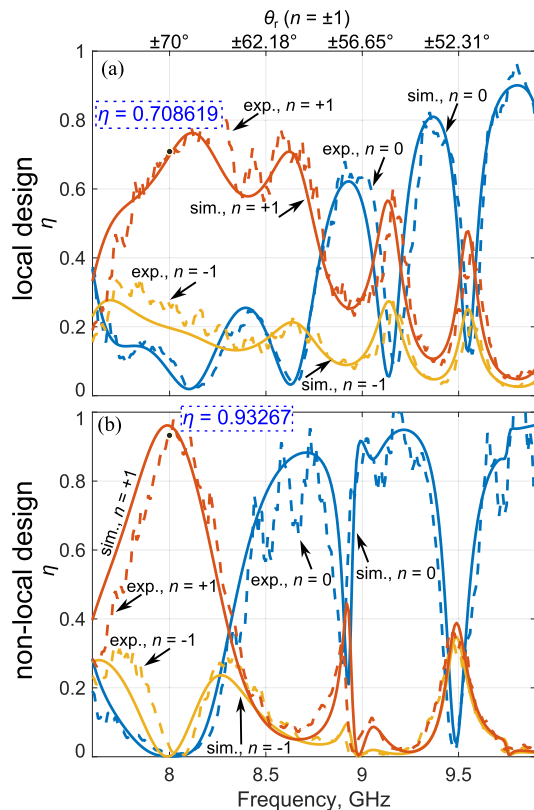


Fig. 8. Scattering efficiency, experimental result, and simulation result for normal illumination: (a) local design and (b) nonlocal design. The additional top  $x$ -axis shows the scattering angle for  $n = \pm 1$  harmonics that corresponds to the processed frequency. Solid lines show simulation data, and dashed lines show data extracted from the measurements.

in the material properties between the actual values and the theoretical assumption.

We also note that the experiment shows that the parasitic scattering from the local design panel in the  $-70^\circ$  direction is stronger than the parasitic specular reflection. In the nonlocal design, all parasitic scattering is effectively suppressed. The measured efficiencies are in line with the results presented in Fig. 7(a) and (c) exactly at the design frequency, or similarly for  $\theta_i = 0^\circ$  in Fig. 7(b) and (d).

It is interesting to note a qualitatively different response of the two metasurfaces at high frequencies, much larger than the design frequency. As expected, when the period of the metasurface does not match the wavelength of the incident wave, the reflection is predominantly in the specular direction, i.e., normal to the plane in the example shown in Figs. 6, 7(a) and (c), and 8. The structure does not exhibit the properties of a diffraction grating, and we see reflections due to surface-averaged currents. However, at some frequencies, the period becomes matched with the wavelength, and we observe sharp drops of reflections into the specular direction. At these frequencies, there is significant scattering into other Floquet harmonics, and observing the red and yellow curves, we can see the intensities of scattering into the corresponding modes. The frequencies of such intensive diffuse scattering are different for the two designs, although the geometrical period of the two patterns is the same. Different structures of the supercells lead to different scatterings far from the design frequency.

Another revealed difference of the response of the two designs is in suppression of specular reflection in the vicinity of the design incidence angle. As is seen in Fig. 7(b) and (d) (blue curves), the nonlocal design results in a wide minimum of specular reflection in the vicinity of  $\theta_i = 0$ , while the local design panel shows two maxima quite close to the design incidence angle. Yet, another peculiarity of the nonlocal design is nearly perfect efficiency of scattering into  $n = -2$  mode at large positive angles of incidence, while for the local design, the efficiency for that mode stays below 50%.

## V. CONCLUSION

In this article, we presented the results of experimental investigations of anomalous reflectors designed as locally periodic phase-gradient reflectors and using numerical optimizations of supercells. All the parameters of the two panels under study were the same except for the lengths of the patches that were tuned using these two different methods. We provided a detailed comparative analysis of these two anomalous reflectors, designed for the same function of anomalous reflection. Combining bistatic and monostatic measurement data, we built 2-D datasets—interpolated reflection maps for each measured frequency point. In the processed results, we investigated the scattered power magnitude from the anomalous reflectors toward specular and anomalous reflections for  $n = \pm 1$  Floquet harmonic orders. Higher harmonics could not be detected due to measurement setup limitations.

While the advantage of the nonlocal design in providing higher efficiencies of anomalous reflection into the design direction and at the design frequency is known and well appreciated, in this work, anomalous reflection efficiency was investigated both for fixed angles toward observation points and toward the propagation directions of different harmonics that depend on the operational frequency. The first set of results is more related to particular engineering solutions demonstrating capabilities of almost perfect anomalous reflection from the reflector designed with nonlocal approach comparing with the local one. We experimentally confirmed that the sample, realized with the nonlocal method, grants not only much more accurate and efficient redirection of the incident power due to better suppression of the parasitic scattering toward undesired directions, but also a similarly wide operational bandwidth as the local design. Our analysis of scattering also demonstrated significant difference of the samples properties in terms of the angular response—illuminated at the angles that are different from the design angle, the structures exhibit totally different trends for all diffraction harmonics. Our analysis also showed quite different behaviors of the structures at higher frequencies outside the design condition. This aspects should be taken into account while engineering anomalous reflectors, where the nonlocal design can bring significant advantages due to much higher efficiency of reflection, especially at extreme angles.

Finally, let us note that there are other platforms for realization of various anomalous reflectors for various frequency ranges, such as arrays of dielectric elements of different shapes (e.g., [17], [18], and many other works). Moreover, there are different physical principles of realizing these effects, such

as the use of metagratings [6] or conventional reflectarrays formed by  $\lambda/2$ -sized unit cells [11], [12]. In the future, it would be interesting and useful to make similar comparative investigations of anomalous reflectors realized in other platforms and using other physical principles.

#### ACKNOWLEDGMENT

The authors thank S. Thurner (DLR) for conducting the measurements.

#### REFERENCES

- [1] A. Epstein and G. V. Eleftheriades, "Synthesis of passive lossless metasurfaces using auxiliary fields for reflectionless beam splitting and perfect reflection," *Phys. Rev. Lett.*, vol. 117, no. 25, Dec. 2016, Art. no. 256103.
- [2] V. S. Asadchy, M. Albooyeh, S. N. Tsvetkova, A. Díaz-Rubio, Y. Ra'di, and S. A. Tretyakov, "Perfect control of reflection and refraction using spatially dispersive metasurfaces," *Phys. Rev. B, Condens. Matter*, vol. 94, no. 7, Aug. 2016, Art. no. 075142.
- [3] V. S. Asadchy, A. Wickberg, A. Díaz-Rubio, and M. Wegener, "Eliminating scattering loss in anomalously reflecting optical metasurfaces," *ACS Photon.*, vol. 4, no. 5, pp. 1264–1270, May 2017.
- [4] A. Díaz-Rubio, V. S. Asadchy, A. Elsakka, and S. A. Tretyakov, "From the generalized reflection law to the realization of perfect anomalous reflectors," *Sci. Adv.*, vol. 3, no. 8, Aug. 2017, Art. no. e1602714.
- [5] D.-H. Kwon, "Lossless scalar metasurfaces for anomalous reflection based on efficient surface field optimization," *IEEE Antennas Wireless Propag. Lett.*, vol. 17, pp. 1149–1152, 2018.
- [6] Y. Ra'di, D. L. Sounas, and A. Alù, "Metagratings: Beyond the limits of graded metasurfaces for wave front control," *Phys. Rev. Lett.*, vol. 119, no. 6, Aug. 2017, Art. no. 067404.
- [7] A. Díaz-Rubio, J. Li, C. Shen, S. A. Cummer, and S. A. Tretyakov, "Power flow–conformal metamirrors for engineering wave reflections," *Sci. Adv.*, vol. 5, no. 2, Feb. 2019, Art. no. eaau7288.
- [8] J. Budhu and A. Grbic, "Perfectly reflecting metasurface reflectarrays: Mutual coupling modeling between unique elements through homogenization," *IEEE Trans. Antennas Propag.*, vol. 69, no. 1, pp. 122–134, Jan. 2021.
- [9] A. Díaz-Rubio and S. A. Tretyakov, "Macroscopic modeling of anomalously reflecting metasurfaces: Angular response and far-field scattering," *IEEE Trans. Antennas Propag.*, vol. 69, no. 10, pp. 6560–6571, Oct. 2021.
- [10] D. Berry, R. Malech, and W. Kennedy, "The reflectarray antenna," *IEEE Trans. Antennas Propag.*, vol. AP-11, no. 6, pp. 645–651, Nov. 1963.
- [11] J. Huang and J. A. Encinar, *Reflectarray Antennas*. Hoboken, NJ, USA: Wiley, 2008.
- [12] P. Nayeri, F. Yang, and A. Z. Elsherbeni, *Reflectarray Antennas: Theory, Designs, and Applications*. Hoboken, NJ, USA: Wiley, 2018.
- [13] D. M. Pozar, S. D. Targonski, and H. D. Syrigos, "Design of millimeter wave microstrip reflectarrays," *IEEE Trans. Antennas Propag.*, vol. 45, no. 2, pp. 287–296, Feb. 1997.
- [14] N. Yu et al., "Light propagation with phase discontinuities: Generalized laws of reflection and refraction," *Science*, vol. 334, no. 6054, pp. 333–337, Oct. 2011.
- [15] V. S. Asadchy et al., "Flat engineered multichannel reflectors," *Phys. Rev. X*, vol. 7, no. 3, Sep. 2017, Art. no. 031046.
- [16] D.-H. Kwon and S. A. Tretyakov, "Perfect reflection control for impenetrable surfaces using surface waves of orthogonal polarization," *Phys. Rev. B, Condens. Matter*, vol. 96, no. 8, Aug. 2017, Art. no. 085438.
- [17] A. S. Kupriyanov, V. V. Khardikov, K. Domina, S. L. Prosvirmin, W. Han, and V. R. Tuz, "Experimental observation of diffractive retroreflection from a dielectric metasurface," *J. Appl. Phys.*, vol. 133, no. 16, Apr. 2023, Art. no. 163101.
- [18] M. Xu et al., "Topology-optimized catenary-like metasurface for wide-angle and high-efficiency deflection: From a discrete to continuous geometric phase," *Opt. Exp.*, vol. 29, no. 7, p. 10181, Mar. 2021.